ORIGINAL ARTICLE

A CFD model with free surface tracking: predicting fill level and residence time in a starve-fed single-screw extruder

Erik Holmen Olofsson[1] · Michael Roland[1] · Jon Spangenberg[1] · Ninna Halberg Jokil[2] · Jesper Henri Hattel[1]

Abstract

Mixing in extrusion is a vital part of achieving consistent and high-quality extrudates, with residence time being an elucidative measure of the mixing performance. Recent studies around numerical modeling of residence time distributions in single-screw extruders appear to consider flooded extruders mainly. This paper introduces a new and general CFD model to characterize the extruder fill length and residence time distribution for a viscoplastic ceramic material in a starve-fed extruder, including free surface tracking. The CFD model simulates a pulse-injection test, where a fluid parcel is injected at the inlet, with subsequent outlet concentration measured over time. The study includes material characterization and model validation based on laboratory tests. Results quantify the impact of accounting for the partially filled extruder instead of assuming it to be flooded, addressing the potential error when only considering simple analytical approximations to calculate system average residence times. Results further show the ability to fit simulation results to more simple analytical models. This underlines the importance of including the entire extrusion system and forming the basis for further work toward enabling real-time model predictions in starve-fed extrusion systems.

Keywords Simulation · Computational fluid dynamics · Residence time · Fill length · Single-screw extruder · Ceramics

1 Introduction

The present study concerns the important industrial process of extrusion of ceramic material by single-screw extruders with metered feeding (starve-fed) [1, 2] as opposed to flooded extrusion. Starve-fed extrusion typically eliminates problems due to bridging and funneling in the feed hopper or slippage on the barrel in the extruder [3].

✉ Erik Holmen Olofsson
  ethol@dtu.dk

  Michael Roland
  mirola@dtu.dk

  Jon Spangenberg
  josip@dtu.dk

  Ninna Halberg Jokil
  nih@topsoe.com

  Jesper Henri Hattel
  jhat@dtu.dk

1 Department of Mechanical Engineering, Technical University of Denmark, Kgs. Lyngby, Denmark

2 R&D Director–Topsoe A/S, Haldor Topsøes Allé 1, DK-2800 Kgs. Lyngby, Denmark

Mixing in extrusion is a vital part of achieving consistent and high-quality extrudates, with strains and frequent particle reorientation through the extruder being the most important influencing factors on the overall flow pattern and hence the final quality of the extrudate. Each fluid element's strain history depends on the shear rate and the processed material residing time inside the extruder [4]. Hence, the residence time is essential for describing the equipment flow pattern and mixing performance [5, 6]. Recent digitalization trends with automated control of continuous manufacturing processes further add to this relevance [7–9]. The nonuniform velocity field over the cross-section of the extruder processing domain results in a complex distribution of strains experienced by the fluid elements. Therefore, the mean residence time is composed of multiple local residence times referred to as the residence time distribution (RTD) [10]. RTD and mean residence time depend on numerous process parameters such as screw speed, feed rate, temperature profile, and screw design [11]. For example, an increased screw speed or feed rate will result in a narrower distribution of local residence times.

Furthermore, the mean residence time is inversely proportional to screw speed and directly proportional to extruder

feed rate [12]. Despite these critical findings, more advanced mathematical modeling of RTD is limited, and consequently, studies relating to RTD mainly explore system-specific characteristics [13, 14]. In general, work around single-screw metered extruders is limited [15], with fill factor predictions consistently relating to twin-screw extruders [16, 17].

Partial filling in stationary operating conditions is an inherent effect of the starve-fed extruder. In this case, the mission of the partially filled section is solely to transport the material to the filled area, and it is only in the filled section that the pressure is built-up for the material to overcome all resistances after leaving the screw [18]. The fill level in the extruder directly affects the resulting RTD. Lower levels are associated with a wider RTD and more shear, whereas higher levels result in a narrower RTD and less shear. Hence, accounting for the degree of fill in the approximation of residence time distributions can improve predictions for optimizing extruder design, operating, and process parameters [19]. However, studies concerning the modeling of partially filled systems are related to twin-screw extruders only [20–22]

There are some interesting numerical studies concerning RTD characterization based on CFD (computational fluid dynamics) [23], DEM (discrete element method) [24, 25], and SPH (smooth particle hydrodynamics) [26] for extruders. In general, the majority of studies model filled extruders, or filled sections of the extruder, where the overall RTD is the cumulative assembly of RTDs from statistically independent sections [27, 28] as initially proposed by Chen et al. [29].

Hence, this paper introduces a general CFD model to simulate the extruder fill length and residence time distribution for a viscoplastic ceramic material in a single-screw, starve-fed pinned extruder at stable operating conditions. Simulations contain the entire extrusion system and account for the fluid-free surface inside the extruder. A Herschel–Bulkley fluid represents the material response, and validation of CFD simulations was based on alignment with extrusion pressures from physical tests. The remainder of the paper is structured as follows: Section 2 introduces the experimental setup and applied material and numerical and analytical models with relevant theory. Section 3 presents and discusses the results, whereas Section 4 summarizes the study's conclusions.

2 Methodology

2.1 Material characterization

The material used during experiments was a mixture of γ-alumina (powder), a binder (powder), and water at room temperature. The binder is a hydroxypropyl methylcellulose (HPMC) [30] thickener, and the porous polycrystalline aluminum oxide [31] agglomerate has an average particle size of 10μm.

The determination of the response curve for the viscoplastic fluid [1], representative of the complex flow characteristics of the material during extrusion, was based on capillary rheometry [32]. A Stable Micro Systems TA.HD plusC instrument [33], with three capillaries of different lengths, was used to register the reaction force based on given piston velocities. Based on a measured density and known piston dimensions and velocity, capillary pressure drop and volume flow can be calculated. The calculated curves are shown in Fig. 1.

The extrusion pressure and volume flow are then converted to respective shear stress and apparent shear rate [32]. Corrections to the apparent measurement data are needed for reliable viscosity data to produce so-called "true" data. In a complete determination, these include Bagley, Mooney, and Weißenberg-Rabinowitsch corrections applied in consecutive order [1]. The Bagley correction separates the actual viscous pressure drop from the capillary entrance and outlet pressure loss. Calculations of apparent shear rates assume Newtonian behavior, where the Weißenberg-Rabinowitsch procedure allows correction for an increased shear rate at the walls due to a pseudoplastic flow behavior. The Mooney correction enables the determination of fluid slipping speed at the wall, which implies a reduced shear rate near the wall [34, 35]. Mooney correction was, however, not considered due to potential practical limitations [36] and uncertainty to the accuracy contribution concerning the magnitude of measurement errors.

A Herschel-Bulkley [37] model representation was preferred to the alternative Bingham [38] relationship due to more accurate modeling of rheological behavior when based on adequate experimental data. Compared to a Bingham fluid, the Herschel-Bulkley model additionally accounts
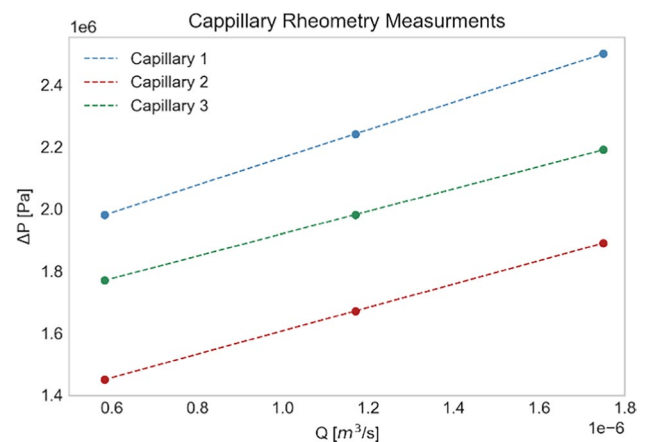

Fig. 1 Curves from capillary measurements using three different capillaries having equal diameter, however different length

for the shear-thinning behavior of a power law fluid. The constitutive Herschel-Buckley equation is given as follows:

$$\tau = \tau_0 + k \cdot \dot{\gamma}^n, \tag{1}$$

where τ is the shear stress, τ_0 is the yield stress, k is the consistency factor, $\dot{\gamma}$ is the shear rate, and n is the dimensionless flow index.

The yield stress, for each capillary, is calculated by fitting linear curves to apparent data in a log–log plot and extrapolating to zero shear rate. Flow indices, for each capillary, are then calculated by fitting power curves to a plot with true shear stress (Bagley corrected) to the apparent shear rate data. The material flow index and yield stress are taken as averages of all three determined flow indices and yield strengths. The consistency factor is determined by fitting one power curve to a plot with true shear stress to true shear rate (Weißenberg-Rabinowitsch corrected) considering the entire measurement data set (data from measurements with all capillaries). Calculated indices and yield stress for Eq. 1 are given in Table 1, and the resulting Herschel-Bulkley material response curve can be seen in Fig. 6 in Section 3.

2.2 Laboratory extrusion tests

A manually fed Diamond America TT100CS-1″ Table Extruder (Fig. 2) with seven barrel pins (pinned extruder) was used for the extrusion tests. The function of the barrel pins is both to avoid rotation and to increase laminar mixing of the processed ceramic material [2]. The extruder was operated with an auger screw without an optional front wiper at a rotational speed of 45 RPM. The barrel was cooled at 22 °C, and temperature and pressure were constantly logged with a Danisco melt pressure transmitter with an integrated thermocouple placed horizontally right before the barrel outlet. Other sensor data logged during tests were water cooling temperature, screw torque, and the total weight of the extrudate. Collected pressure and extrudate weight data displayed in Fig. 7 were continuously logged with a computer with a frequency of 1 second. The flange had one die, and the extruded paste was prepared using a sigma blade batch mixer. The die (capillary) had a respective diameter
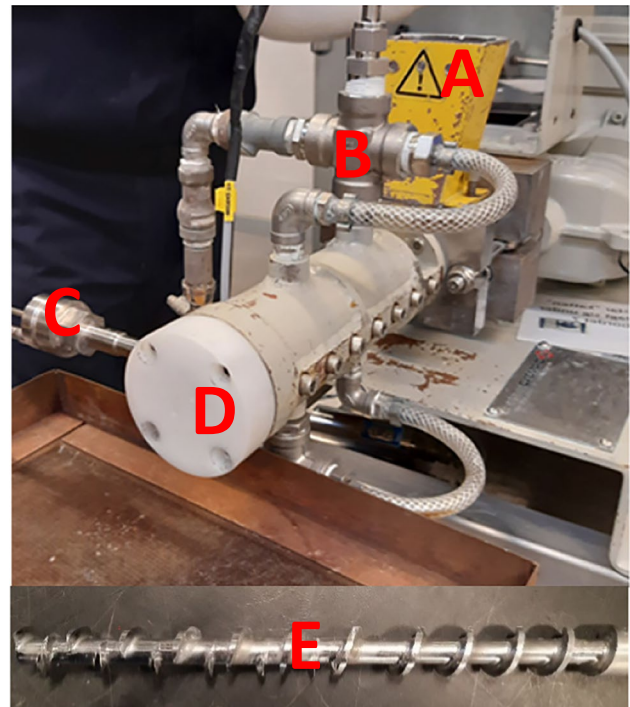

Fig. 2 System setup for the considered extrusion tests, including the following: **A**—hopper, **B**—barrel cooling system with temperature sensor, **C**—paste pressure and temperature transmitter, **D**—die flange, and **E**—auger screw

and length of 3.0 and 24.75 mm. The auger screw had a constant diameter of 25.4 mm and a root diameter of 12.7 mm. The L/D-ratio of the auger screw is 8:1 and 70% of the total length consisting of the compressive and metering zone with a slightly shorter pitch [39].

Manual feeding implied that a prepared mix of material was repeatedly deposited into the hopper of the extruder using a spoon. During the test, the extruder was operated, resembling a fully filled state. This was accomplished by manually feeding until visually detecting slight flooding at the barrel inlet and, from there on, adapting the frequency of filling to maintaining this state when logging sensor data.

Starve-fed extruders at stationary operating conditions will inherently be partially filled and therefore characterized by a fully- and partially filled zone. The fill length (L_{fill}) specifies the distance over which the extruder is fully filled, as shown in Fig. 3.

The extruder is considered filled when the entire barrel section, constituted by the length from K_L to K_0 (Fig. 3) of the extruder, is filled.

In a pulse input experiment, an amount of tracer fluid is rapidly injected at the inlet, followed by a measurement of the tracer concentration (C) at the outlet over time (Fig. 4).

The residence time distribution for a pulse input is generally defined as [22]

Table 1 Material model properties used in numerical simulations

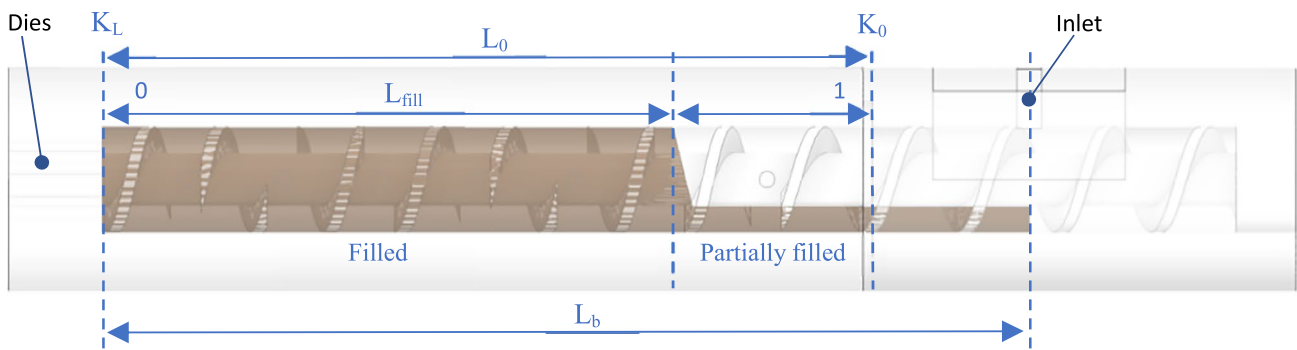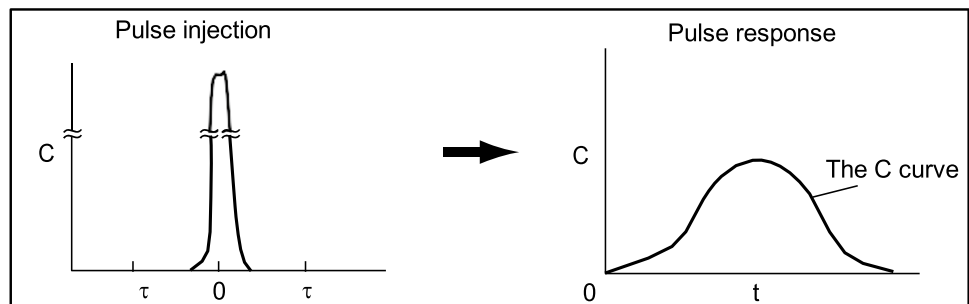| Symbol	Value	Unit
ρ	1404	kg·m^{-3}
n	0.212	–
τ_0	$1.74e{+}05$	Pa
μ_{max}	5861.84	Pa·s
$\dot{\gamma}_{min}$	59.34	s^{-1}
k	73,251	Pa·s^n
g	9.82	m·s^{-2}

Fig. 3 Extruder barrel with indicated fill length (L_{fill}) marking the transition from the filled to the partially filled zone

Fig. 4 Characteristic injection and response curves from a pulse input experiment, with τ representing an expected residence time

$$E(t) = \frac{C(t)}{\int_0^\infty C(t)dt} = \frac{C(t)}{\sum_0^\infty C(t)\Delta t}, \quad (2)$$

where $C(t)$ represents the given tracer concentration. The residence time distribution function $E(t)$ is a measure of the time different fluid elements spend inside a system, where $E(t)dt$ gives the fraction of fluid having left the reactor within the considered time frame dt. The fraction of all the fluid that has resided in the system between $t=0$ and $t=\infty$ is 1. Based on a pulse experiment, the average residence time can then be calculated as follows:

$$\bar{t}_{tracer} = \int_0^\infty tE(t)dt = \frac{\sum_0^\infty tC(t)\Delta t}{\sum_0^\infty C(t)\Delta t}. \quad (3)$$

RTD curves of an extrusion process are typically represented by a pattern consisting of an initial delay time, followed by a rise in the concentration of tracer particles, and finally ending with a gradual tail. The initial delay time represents the fluid plug flow behavior, and the tail represents the level of redundant processing influencing the product quality.

2.3 Analytical modeling

Based on the given characteristics, two models assuming plug flow followed by a series of continuous stirred tank reactors (CSTRs) [40] were considered to verify the

numerical model output and the potential applicability. The only difference between the considered models is that, in the first case, the CSTRs are assumed to include a dead volume fraction, whereas in the latter they are not.

The first analytical model, including a dead volume, is given as follows [41]:

$$E(\theta) = \frac{b\left[b(\theta - p)\right]^{n-1}}{(n-1)!} \exp\left[-b(\theta - p)\right], \quad (4)$$

where $b = n/(1-p)(1-d)$, $p = t_{min}/t$ and $\theta = \bar{t}/t$. The parameter p represents the fraction of plug flow where θ is the dimensionless time, n is the number of CSTRs and t_{min} is the initial time of measurable tracer at the outlet. The second model, without a dead volume, is formulated as follows [42]:

$$E(t) = \frac{1}{\bar{t} - p\bar{t}}n(\theta)^{n-1}\frac{1}{(n-1)!}e^{-n(\theta)}, \quad (5)$$

where $\theta = (t - p\bar{t})/(\bar{t} - p\bar{t})$ and $E(t)=0$; for $0 \leq \theta \leq p$.

For practical purposes, the average residence time is often simply approximated by the following:

$$\bar{t}_{filled} = \frac{V}{Q} \quad (6)$$

where Q represents the volumetric flow rate and V is the used free volume of the extruder [3]. Strictly speaking, Eq. (6) is valid for a pipe plug flow in which all fluid particles would

experience the same residence time. Further, note that the used free volume (V) might encompass a smaller section of the extruder free volume, V_0, which is the resultant space between the auger screw and the barrel wall available for the processed material. That is, the free volume defines the maximum capacity of the extruder. An approximation of the free volume can be calculated as follows [3]:

$$V_0 = A_0 L_b, \tag{7}$$

where A_0 is the screw open area (cross-sectional area between barrel and screw shaft) and L_b is the length of the referenced barrel section. A_0 can further be calculated as

$$A_0 = A_b - A_s, \tag{8}$$

where A_b and A_s are barrel and screw cross-sectional areas, respectively. Ignoring the area occupied by the screw flights, both barrel, and screw cross-sectional areas can be expressed by screw root and barrel diameters according to

$$A_b = \frac{\pi D_b^2}{4} \tag{9}$$

and

$$A_r = \frac{\pi D_r^2}{4}, \tag{10}$$

where D_b is the barrel diameter and D_r is the screw shaft diameter. By substituting Eqs. (9) and (10) into (7), a simplified expression of the free volume can be derived as

$$V_0 = \frac{\pi}{4}\left(D_b^2 - D_s^2\right) L_b \tag{11}$$

With the assumption of the entire free volume of the system being utilized, Eq. (11) can be substituted into Eq. (6), resulting in an approximation of the average RTD according to

$$\bar{t}_{filled} = \frac{\frac{\pi}{4}\left(D_b^2 - D_s^2\right) L_b}{Q}. \tag{12}$$

As considered systems are starve-fed, with an auger screw speed sufficient to remove all the material being fed, the entire barrel section will not be fully utilized. Hence, for these types of systems, V will not correspond to V_0 and the application of equation (12) will be susceptible to an error of a size that is relative to the actual fill level of the extruder system.

Verges (2011) [43] proposed an expression for calculating the average residence time for a starved Ko-kneader according to the following:

$$\bar{t} = \frac{A}{Q} + \frac{B}{N}, \tag{13}$$

where

$$A = Q\frac{N_2\bar{t}_2 - N_1\bar{t}_1}{N_2 - N_1}, B = N_1 N_2 \frac{\bar{t}_2 - \bar{t}_1}{N_2 - N_1}.$$

N_1 and N_2 correspond to two different auger rotational speeds. Note that even though these expressions are originally given for a starved Ko-kneader[43], they are proposed to apply to the considered extruder system in the present work.

2.4 Numerical model

The CFD model considers the continuous processing of viscoplastic ceramic material. The flow is assumed to be laminar, and the fluid is further regarded as incompressible and isothermal. As the Herschel-Bulkley model implies that the viscosity diverges towards infinity as the strain rate approaches zero, it is numerically implemented with an upper limit according to

$$\mu(\dot{\gamma}) = \begin{cases} \mu_\infty & \text{for } |\tau| \leq \tau_0, \\ \mu_\infty + k|\dot{\gamma}|^{n-1} & \text{for } |\tau| > \tau_0 \end{cases}, \tag{14}$$

where μ_∞ represents the limiting viscosity and τ_0 the yield stress. With shear stress directly dependent on share rate, Eq. (13) can alternatively be given as

$$\mu(\dot{\gamma}) = \begin{cases} \mu_{max}, & \text{for } |\dot{\gamma}| \leq \dot{\gamma}_c \\ \tau_{max}|\dot{\gamma}|^{-1} + k|\dot{\gamma}|^{n-1} & \text{for } |\dot{\gamma}| > \dot{\gamma}_c \end{cases}, \tag{15}$$

where $\dot{\gamma}$ corresponds to the fluid shear rate, μ_{max} the maximum apparent viscosity and $\dot{\gamma}_c$ the critical shear rate. The maximum shear stress (τ_{max}) is given as

$$\tau_{max} = \tau_0 + k|\dot{\gamma}_{max}|^n, \tag{16}$$

where

$$|\dot{\gamma}_{max}| = \begin{cases} 10^6 & |\dot{\gamma}_{min}| = 0 \\ 10^6 \bullet |\dot{\gamma}_{min}| & |\dot{\gamma}_{min}| \geq 0 \end{cases} \tag{17}$$

Here, $|\dot{\gamma}_{min}|$ corresponds to the minimum specified strain rate specified in the CFD software.

The numerical problem is solved based on the continuity and momentum equations, respectively:

$$\boldsymbol{\nabla} \cdot \boldsymbol{u} = 0 \tag{18}$$

$$\rho\left[\frac{\partial \mathbf{u}}{\partial t} + (\boldsymbol{u} \bullet \boldsymbol{\nabla})\boldsymbol{u}\right] = -\boldsymbol{\nabla}p + \rho\mathbf{g} - (\boldsymbol{\nabla} \bullet \boldsymbol{\sigma}), \tag{19}$$

where $\boldsymbol{g} = (0, g, 0)$ corresponds to the constant gravitational vector, ρ is the constant density, p the pressure, and $\boldsymbol{\sigma}$ the material deviatoric stress tensor defined as

$$\boldsymbol{\sigma} = 2\mu(\dot{\gamma}, T)\boldsymbol{D}. \tag{20}$$

$\boldsymbol{D}$ is further the deformation rate tensor defined as

$$\boldsymbol{D} = \frac{1}{2}\left(\boldsymbol{\nabla}\boldsymbol{u} + (\boldsymbol{\nabla}\boldsymbol{u})^T\right) \tag{21}$$

Simulations were conducted in the commercial CFD software Flow-3D [44], where the finite volume method is used to solve continuity and momentum equations (18, 19), and the position of the free surface is calculated with the volume of fluid technique (VOF) [45]. The

Initial simulations to investigate the fidelity of the numerical model were carried out with the corresponding configurations for the laboratory extrusion tests (Section 2.2), i.e., similar dimensions, number of dies, and auger rotational speed, as stated before Fig. 2. Further simulations used the same configuration, however, with eight dies. To ensure a continuous deposition into the extruder, a narrow-squared channel positioned at the center of the hopper was used to feed fluid into the extruder. A point probe, representing the response from the physical pressure/temperature sensor, was placed in the center of the modeled geometrical cavity arising from the space between the sensor membrane and the barrel wall (Fig. 5). The computational domain was meshed with a uniform discretization of cells. The total screw torque was approximated based on the sum of its reacting forces and an assumption of a mass density of steel at 7850 kg/m³. CAD geometries and numerical domain can be seen in Fig. 5.

The material properties used in the simulations are given in Table 1. Values for $\dot{\gamma}_{min}$ and μ_{max} are calculated using the power law model with reference to τ_0. Density was calculated as an average of three water displacement measurements on different extrudates during laboratory extrusion tests (Section 2.2).
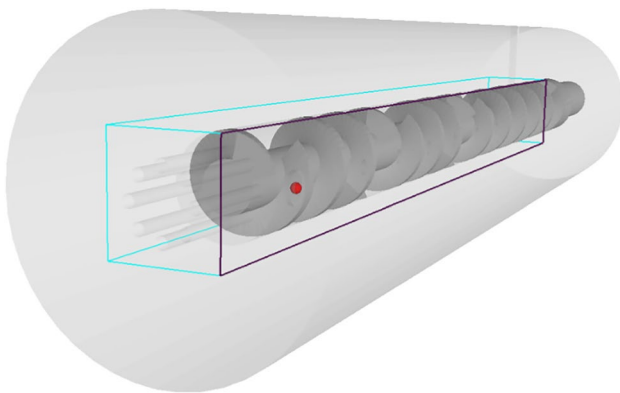

Fig. 5 Solid geometries (auger screw and barrel) imported as STL files in the simulation software. The framed box represents the discretized domain, and the red sphere is the position of a data logging point for pressure measurements

Predictions using the CFD model are based on executing a simulation in two consecutive steps:

1. In the first step, the model is initiated and simulated until reaching a quasistatic state characterized by a pressure-based convergence criterion per time step below 1%.
2. In the second step, the model is restarted from the converged step while initiating a pulse input experiment injecting 0.06 cm³ ($6e^{-8}$ m³) of tracer fluid with a concentration of 100 kg/m³ at the inlet.

Fill length was calculated by postprocessing the first step and based on exported cell fill fractions. RTD was calculated by postprocessing the second step and based on exported tracer concentrations from all die outlet surfaces. A script was used to automatically format and export the fill fraction and tracer concentrations to Python where main calculations were done and figures generated. A more detailed description to the postprocessing calculations is presented under the next section.

2.5 Numerical postprocessing

The average fill fraction of a cross-sectional layer at any distance along the barrel z-axis is naturally defined as

$$\boldsymbol{F}(z) = \frac{1}{A(z)}\sum_{A(z)}\boldsymbol{f}(x, y)\Delta x\Delta y \tag{22}$$

where f represents the fill fraction of each numerical cell and z is the distance from the die plate denoted K_L in Fig. 3. From the resulting vector of fill fractions, the coordinate (K_{fill}) approximating a filled extruder was subsequently defined as

$$K_{fill} = z\big(F_i \geq 95\%\big) \begin{cases} \text{where} & F_{(i+1)} \geq 95\% \\ \text{and} & F_{(i-1)} < 95\% \end{cases}, \tag{23}$$

where i corresponds to the index of considered cross-sectional layers, when iteratively moving from the inlet towards the exit of the extruder. Lastly, the fill length was normalized according to the barrel position as

$$L_{fill} = \frac{K_L - K_{fill}}{K_L - K_0}, \tag{24}$$

where K_L and K_0 represent the z-axis coordinates of the barrel section's respective start and end coordinates (Fig. 3).

The concentration was first averaged over the Flow-3D data logging points positioned at the die outlet as

$$\boldsymbol{C}(t) = \frac{\sum_1^n C_i(t)}{n}, \tag{25}$$

where n represents the number of data logging points. The residence time distribution (E) was then calculated according to Eq. (2), whereas the average residence time using the scalar tracing fluid was calculated according to Eq. (3), and average residence time by Lagrangian particle tracking was calculated as

$$\bar{t}_{particles} = \frac{\sum_1^n t_i(outlet)}{n}, \tag{26}$$

where $t(outlet)$ represents the particle time at the die outlet and n is the number of particles processed.

To verify the simulation model against Eq. (12), a simulation was run with a fully filled barrel section, and the average residence time based on the fluid tracer was compared to the analytically calculated value.

3 Results and discussion

3.1 Material characterization

Figure 6 shows the resultant Herschel-Bulkley model created by entering values in Table 1 in Eq. 1. Hence, fluid motion is not produced until the given yield stress is reached and the flow index is indicative of a quite strongly pseudoplastic material with considerable decrease in apparent viscosity with increasing shear rate.

3.2 Laboratory extrusion tests

Figure 7 shows measurement results from laboratory tests described under Section 2.2, where the logged pressure is overlaid by the accumulated extrudate's weight over roughly three minutes of extrusion. The figure includes two

sequential experimental tests based on the same batch of prepared material. The extrudate was continuously collected in a bucket standing on a scale, hence the continuously linearly increasing weight curves. Local fluctuations in the pressure signal relate to material inhomogeneity, and the global fluctuations are a result of inconsistent filling by the operator when manually depositing material into the extruder. The given average extrusion pressure is, for each consecutive test, taken as averages for all data points displayed in Fig. 7. The average pressures for tests 1 and 2 were 25.64 and 27.25 Bar, respectively. An approximated volume flow was based on measured density, total extrudate weight, and the total time for collecting the extrudate weight data.

3.3 Numerical results

Figure 8 shows a snapshot of the transient CFD simulation running at a quasistatic state, where the material is continuously deposited through a vertical square tube positioned at
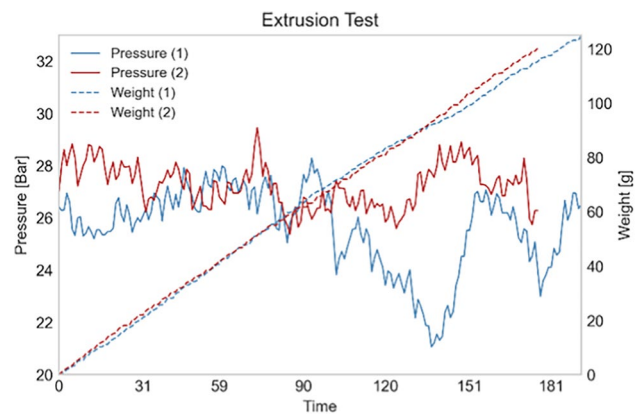

Fig. 7 Experimental data (extrudate weight and extrusion pressure) from laboratory tests

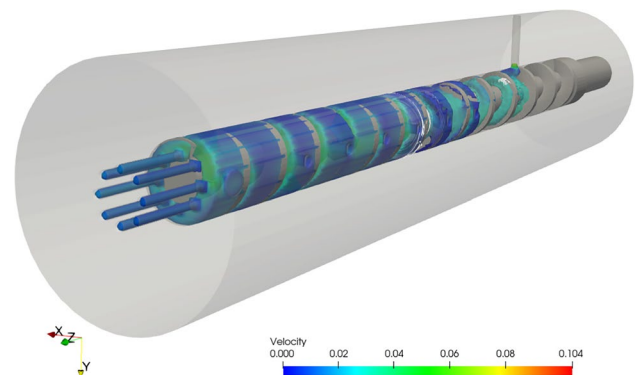**Fig. 6** Herschel-Buckley material response curve based on capillary rheometry test data

Fig. 8 A 3D snapshot of the simulation running with a dimensionless throughput $\bar{Q}= 0.019$. The contour represents the velocity in meter per second

Fig. 9 An axial 2D-snapshot (same time frame as Fig. 8) of the simulation at dimensionless throughput $\bar{Q}$= 0.02. The contour represents the gauge pressure in Pascal
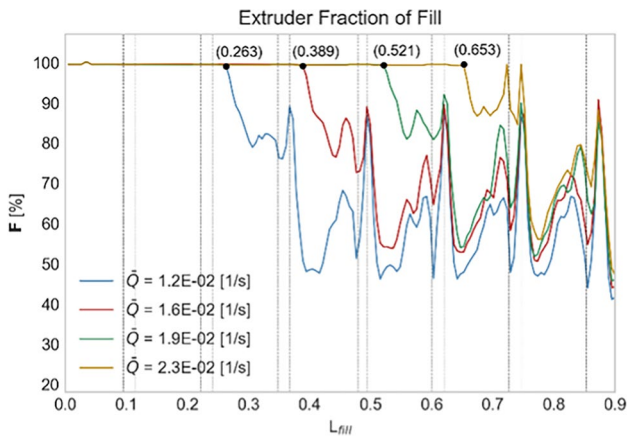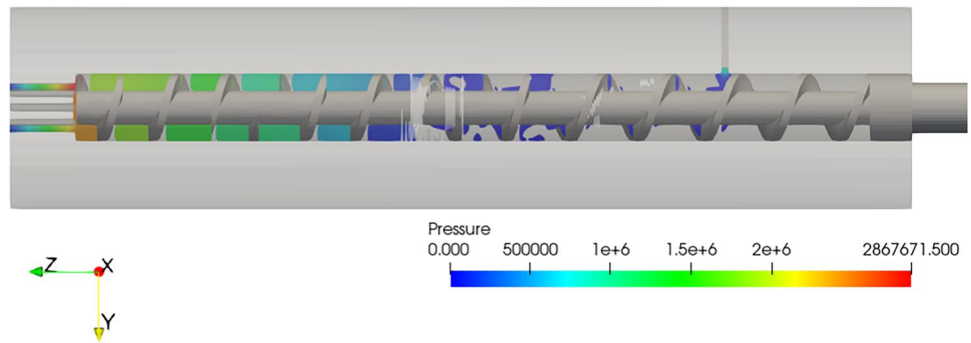

Fig. 10 The fill fraction (**F**) along the extruder and the determined fill length (L_{fill})
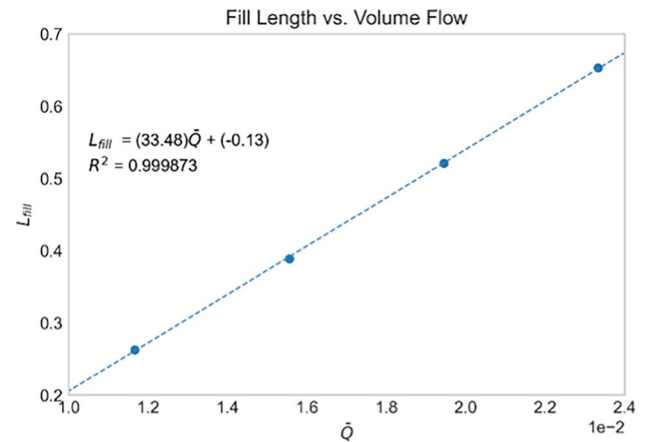

Fig. 11 Plot of dimensionless flow rate to fill length. Included is also the equation of the linear function and its R^2 value

the center of the hopper position. The blue surface is based on the no-slip wall condition, hence the velocity being zero at the walls. The white-colored streamlines are indicating areas where the fluid speed is relatively high, which is mainly around the mixing pin where the free surface is located. This is perhaps even better illustrated in Fig. 9.

Figure 9 shows the pressure in a 2D-plane at the center axis of the extruder. It is seen that the pressure builds up more or less linearly, starting from the position where the starved extruder becomes fully filled. This simulation corresponds to the fill fraction represented by the green curve in Fig. 10, where the level of fill (L_{fill}) is predicted to be 0.526. Hence, about half of the extruder is fully filled at the current extruder operating conditions.

Figure 10 shows the fill fraction over the extruder for the case with eight dies at varying dimensionless throughputs ranging from 0.012 to 0.023 [1/s]. The result is based on data generated according to simulation step 1, as described in Section 2.4. The fill fraction (**F**) for each throughput can be seen fluctuating with an increase around every mixing pin. The black markers indicate the positions where the fill fraction is predicted to reach 100%, and the alongside values represent the predicted value of L_{fill}. Vertical dashed lines in

the figure mark the position of the mixing screws, emphasizing the influence on the fill fraction. The x-axis represents the dimensionless level of fill according to Fig. 3, where a fill of 0.5 would imply that the level of fill is predicted to be located precisely halfway between K_L to K_0.

Figure 11 shows a plot of the fill length versus dimensionless flow rate, where the fill length increases somewhat linearly with an increasing flow rate. It can be noticed that, if extrapolated, the linear model predicts an unphysical negative fill at zero throughputs. This underlines that the proposed linear model should only be used within the region of consideration.

To clarify the predicted fill lengths and results in Fig. 10, Fig. 12 visualizes the extruder geometry with bullets marking the locations of the determined K_{fill}, i.e., the position along the extruder where the fill fraction exceeds 95 percent for different throughputs.

Figure 13 shows the pressure at different fill lengths from the simulation model and that the model predicts a pressure of 28.32 Bar for the filled state corresponding to the state of the extrusion tests in Fig. 7.

Hence, when comparing the pressure (28.32 Bar) determined from simulations with the average, measured
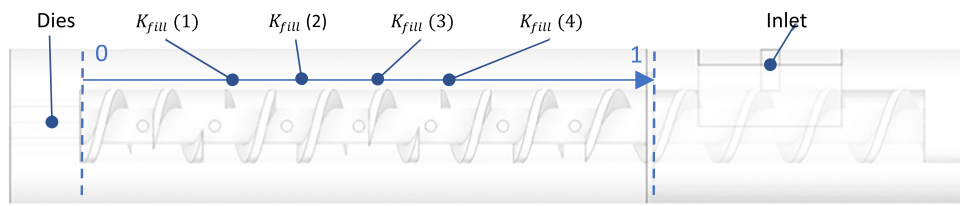
Fig. 12 The geometry showing locations of calculated K_{fill} coordinates. Given locations correspond to the following levels of fill (L_{fill}) and normalized throughputs ($\overline{Q}$): K_{fill} (1): ($L_{fill} = 0.266$, $\overline{Q} = 1.2E - 2$), K_{fill} (2): ($L_{fill} = 0.393$, $\overline{Q} = 1.6E - 2$), K_{fill} (3): ($L_{fill} = 0.526$, $\overline{Q} = 1.9E - 2$), K_{fill} (4): ($L_{fill} = 0.659$, $\overline{Q} = 2.3E - 2$)
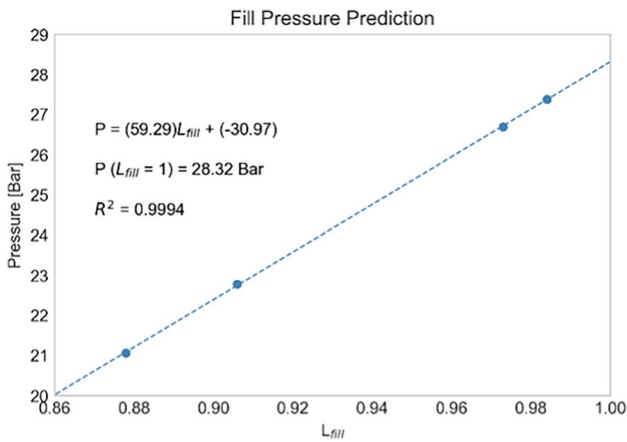

Fig. 13 Extrusion pressures at different flow rates for the simulation model
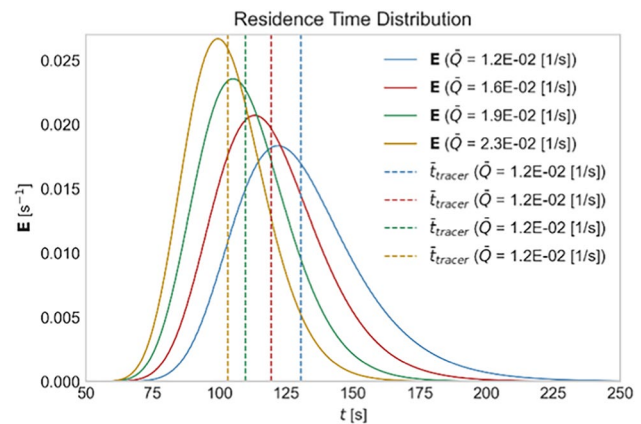
Fig. 14 Plot of residence time distribution at different inlet flow rates where vertical lines indicate average residence time

pressures from tests (Fig. 7), there is a respective deviation of 9.46% (25.64 Bar) and 3.78% (27.25 Bar). The accuracy is quite satisfying, considering potential limitations in relation to model resolution, boundary conditions, experimental errors, equipment wear, temperature effects, and wall slippage.

Figure 14 shows the tracer fluid residence-time distribution curves for the four different considered flow rates. The included vertical dashed lines indicate the $\bar{t}_{tracer}$ value for each RTD curve.

The result corresponds to the output from simulation step 2, as described in Section 2.4. The model confirms previous studies showing a narrower distribution and shorter average residence time with an increased extruder feed rate [12]. The tighter RTD and shorter $\bar{t}_{tracer}$ is mainly based on an increased throughput, which reduces cross-channel flow. Cross-channel flow does not contribute to the net positive movement of material along the extruder barrel, but instead re-circulates it within the screw flights causing material mixing.

Table 2 shows the complete data set of filling length as well as the average residence time based on the three different approaches: (i) $\bar{t}_{filled}$ (analytical), (ii) $\bar{t}_{tracer}$ (scalar tracer), and (iii) $\bar{t}_{particles}$ [s] (particle tracer).

Table 2 Data corresponding to flow rate and average residence times

$\overline{Q}$ [1/s]	L_{fill} [1]	$\bar{t}_{filled}$ [s]	$\bar{t}_{tracer}$ [s]	$\bar{t}_{particles}$ [s]/particles
0.012	0.266	113.65	132.34	119.19/9
0.016	0.393	85.24	118.86	107.07/11
0.019	0.526	68.19	109.57	105.50/10
0.023	0.659	56.83	103.74	99.54/18

It can be noted that the $\bar{t}_{filled}$ and $\bar{t}_{particles}$ consistently underpredict the average residence time as compared to $\bar{t}_{tracer}$. 37 Lagrangian particles were initiated at the inlet for each simulation, but only a portion of these was used to calculate $\bar{t}_{particles}$. This was due to the particles occasionally getting stuck when reaching a zero-velocity boundary in nonfilled areas of the domain. Hence, the number of particles being used for the particle-based filling time is also shown in column five of table 2. The table shows that a higher level of fill resulted in more processed particles and that $\bar{t}_{particles}$ consistently converged towards $\bar{t}_{tracer}$. This contributed to the validation of the scalar tracer result.

Fig. 15 Tracer average residence time based on numerical simulation (blue) and theoretical (red) based on equation 13. The left figure is based on varied throughput at constant auger rotational speed (RPM = 45). The right figure is based on varied auger rotational speeds at constant throughput ($\overline{Q} = 0.019$)
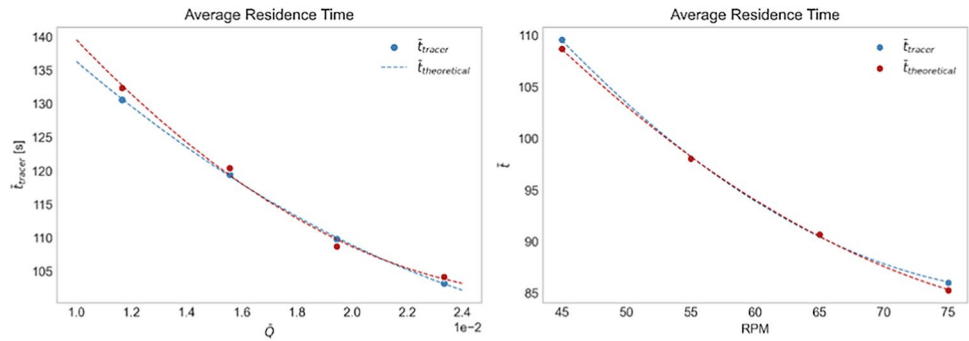
3.4 Numerical to analytical comparison

Figure 15 shows predictions of average residence time. The blue curves $(\overline{t}_{tracer})$ represent an exponential fit of data points calculated individually based on the numerical model. The red line $(\overline{t}_{theoretical})$ represents an exponential fit towards data points calculated according to equation (13). In the rightmost figure, constants A and B were calculated based on numerical results, which corresponds to auger rotational speeds $N_1 = 55$ and $N_2 = 65$ and a constant throughput of $\overline{Q} = 0.019$. These constants were then used when calculating all data points.

However, in the leftmost figure, each prediction according to Eq. (13) corresponds to an individual A and B constant. That is, for each considered throughput, A and B constants were exclusively calculated based on a variation of auger rotational speeds $N_1 = 55$ and $N_2 = 65$.

To allow for a continuous material deposition into the extruder, the dimensions of the inlet, as compared to the actual size in the physical system inlet, needed to be reduced. This resulted in the material being deposited over a limited area on top of the screw, as compared to the considered physical system. The reduced inlet had sides corresponding to 12% of the auger screw diameter. A consequence of the modified inlet was that the position of flights at time of the pulse injection was observed to slightly influence the output. Hence, some discrepancies in the model output should be expected based on nonconsistencies in the alignment of the auger screw when initiating the pulse injection simulations.

Figure 16 shows the deviation (error) of the analytically calculated residence time $(\overline{t}_{filled})$ relative to a numerically predicted value $(\overline{t}_{tracer})$. The free volume for the analytical prediction was based on Eq. (11), with L_b representing the numerically predicted fill length.

The difference of the analytical $(\overline{t}_{filled})$ model and the numerical $(\overline{t}_{tracer})$ is linearly decreasing with increasing fill level and the linearly fitted function approximates a relative difference of −10% at a fully filled extruder ($L_{fill} = 1$). It was, however, noted that if using the exact free volume reported by the CFD software in the analytical expression,
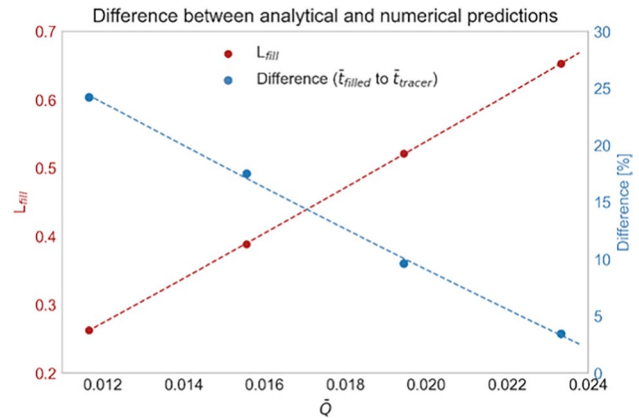

Fig. 16 Fill length and relative difference between $\overline{t}_{filled}$ and $\overline{t}_{tracer}$ as a function of volume flow
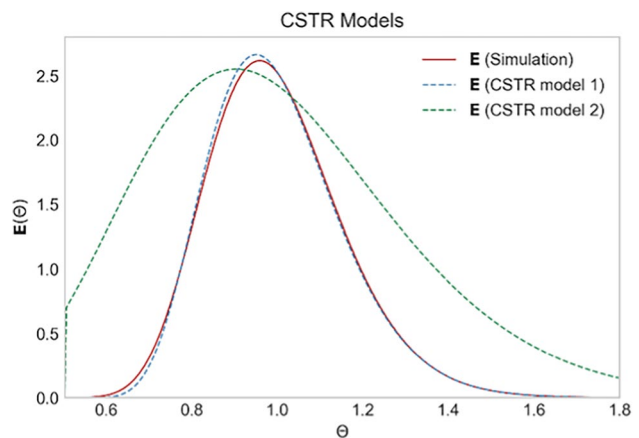

Fig. 17 CSTR models fitted to a RTD curve produced by the simulation model ($\overline{Q} = 0.019$ and 45 RPM)

there was a perfect match between the numerical and analytical predictions.

Figure 17 shows the two CSTR models (Eqs. (4) and (5)) fitted to the numerical approximation to verify and investigate the ability to represent system residence time distribution using an empirical model fitted to a reduced

simulation data set. The RTD originates from a simulation trace injection test having dimensionless throughput $\overline{Q} =$ 0.019 and an auger screw rotational speed of 45 RPM. Fitting was done by minimizing the root mean squared error (RSME):

$$\text{RMSE} = \left[\sum_{i=1}^{N} \left(y_i - f(x_i) \right)^2 / N \right]^{1/2},$$

where y_i is the numerical data and $f(x_i)$ is the representative CSTR model data.

The RMSE values, from the best possible fit produced for CSTR models 1 and 2, were 2.18 and 8.29, respectively. Therefore, it was concluded that model 1 would be the preferable model for the considered application.

Figure 18 shows model 1 fitted to the numerically approximated residence time distribution at varying throughput (leftmost figure) and auger rotational speed (rightmost figure). Despite some minor deviations, the CSTR curves can be seen as consistently representative of the numerical model curves at varying process parameters. This emphasizes the general usability for the application of the CSTR model l. It can further be noted that each figure contains the simulation RTD in Fig. 17 (dark red curve), which was considered for model comparison.

Figure 19 shows a linear fit between the considered numbers of CSTRs (*n*) for the respective residence time distributions considered in Fig. 18. This indicates that two numerical data points would be sufficient for the considered CSTR model to predict distributions at any given throughput or auger rotational speed.

Results show that a successful procedure has been found to systematically predict the starved-fed extruder's fill length and residence time distribution, where the effect of varying controllable process parameters, such as auger rotational speed and throughput, is of solid relevance due to their correlation to product quality attributes. For the case of the considered system, results further allow the fitting of reduced-order empirical models representing the system response based on varying throughput and auger rotational speed.

4 Conclusions

In this study, we have presented a methodology that uses an advanced CFD model for starved extrusion simulations, allowing for predicting residence time based on the fill length position. The work has been validated for the case of a ceramic viscous-plastic fluid in a pinned single-screw starve-fed extruder, incorporating the complete extruder processing domain. The validation was based on physical pressure measurements and the verification by comparison with analytical solutions for average residence time and residence time distribution based on well-accepted expressions from the literature. The system response was determined throughout the study based on four numerical data points. For model

Fig. 18 Model 1 (CSTR) fitted to numerical approximations at varying throughput (left) and auger rotational speed (right)
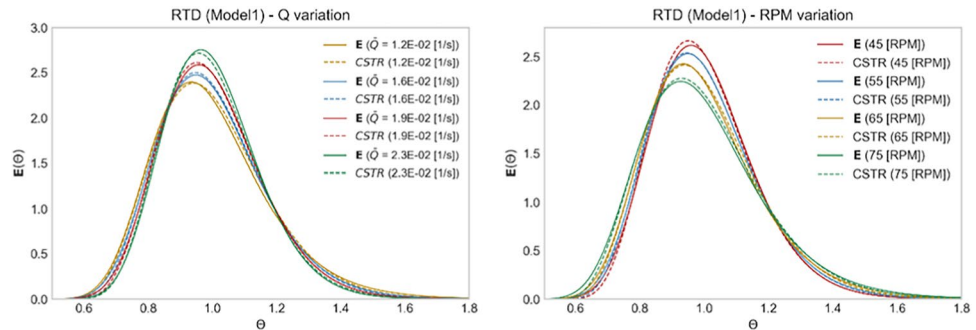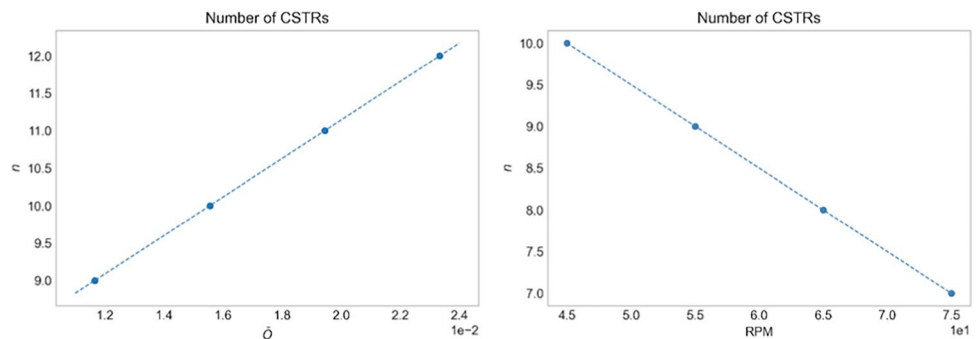

Fig. 19 Number of CSTRs when varying throughput (left) and auger rotational speed (right)

verification purposes, this would also be recommended for any further system characterizations. The work confirmed the validity of a simplified analytical expression for predicting the average residence time of a fully filled system and quantified the potential magnitude of error when assuming a starved extruder to be fully filled.

The simulations provided a characteristic system response, with respect to varying screw speed or feed rate. However, the residence time distribution is highly affected by the stationary state of the system, which, when entering a material over a highly reduced area, was found to be slightly affected by the screw rotational position. Therefore, some care should be taken with respect to the position of the screw when initiating trace injection. More accurate estimations of the residence time can probably be achieved by introducing material that covers a greater portion of the extruder hopper.

Fitted empirical models that include a dead volume were demonstrated to be valid and applicable for predicting the residence time distribution. Four CFD simulations (two data points for the corresponding level of fill and residence time) were sufficient to fit analytical models for a general description of system fill, residence time, and average residence time for any throughput and auger rotational speed. This may be relevant for enabling demonstrated approach to be used as a basis for more accurate real-time predictions and process optimization [46–48].

The overall conclusion is that the work conducted enables the determination of the fill length position, further allowing for enhanced predictions of the residence time distributions in starve-fed extruders. Based on a CFD model encompassing the entire extruder system, the methodology further provides a comprehensive tool for design exploration.

Declarations

Competing interests The authors declare no competing interests.

References

1. Händle F (2007) Extrusion in ceramics. Springer, Berlin, New York
2. Händle F (2019) The art of ceramic extrusion, 1st edn. Springer International Publishing: Imprint: Springer, Cham
3. Giles HF, Wagner JR, Mount EM (2005) Extrusion: the definitive processing guide and handbook. William Andrew Pub, Norwich, NY
4. Kiana K (2011) Quantitative parameters to evaluate mixing in a single screw extruder. McGill University
5. Danckwerts PV (1995) Continuous flow systems. Distribution of residence times. Chem Eng Sci 50:3855. https://doi.org/10.1016/0009-2509(96)81810-0
6. Bhalode P, Ierapetritou M (2020) A review of existing mixing indices in solid-based continuous blending operations. Powder Technol 373:195–209. https://doi.org/10.1016/j.powtec.2020.06.043
7. Gyürkés M, Madarász L, Záhonyi P et al (2022) Soft sensor for content prediction in an integrated continuous pharmaceutical formulation line based on the residence time distribution of unit operations. Int J Pharm 624:121950. https://doi.org/10.1016/j.ijpharm.2022.121950
8. Chen Y, Yang O, Sampat C et al (2020) Digital twins in pharmaceutical and biopharmaceutical manufacturing: a literature review. Processes 8:1088. https://doi.org/10.3390/pr8091088
9. Dosta M, Litster JD, Heinrich S (2020) Flowsheet simulation of solids processes: current status and future trends. Adv Powder Technol 31:947–953. https://doi.org/10.1016/j.apt.2019.12.015
10. Kim SJ, Kwon TH (1996) Measures of mixing for extrusion by averaging concepts. Polym Eng Sci 36:1466–1476. https://doi.org/10.1002/pen.10541
11. Yeh A-I, Jaw Y-M (1998) Modeling residence time distributions for single screw extrusion process. J Food Eng 35:211–232. https://doi.org/10.1016/S0260-8774(98)00001-6
12. Bi C, Jiang B, Li A (2007) Digital image processing method for measuring the residence time distribution in a plasticating extruder. Polym Eng Sci 47:1108–1113. https://doi.org/10.1002/pen.20793
13. Gao Y, Muzzio FJ, Ierapetritou MG (2012) A review of the Residence Time Distribution (RTD) applications in solid unit operations. Powder Technol 228:416–423. https://doi.org/10.1016/j.powtec.2012.05.060
14. Nastaj A, Wilczyński K (2020) Optimization for starve fed/flood fed single screw extrusion of polymeric materials. Polymers 12:149. https://doi.org/10.3390/polym12010149
15. Bizhanov AM, Podgorodetskii GS (2020) On the movement of briquetted mass in extruder. Exact Solutions. 1. Steel Transl 50:1–5. https://doi.org/10.3103/S0967091220010027
16. Bawiskar S, White JL (1997) A composite model for solid conveying, melting, pressure and fill factor profiles in modular co-rotating twin screw extruders. Int Polym Process 12:331–340. https://doi.org/10.3139/217.970331
17. Wilczynski K, Jiang Q, White JL (2022) A composite model for melting, pressure and fill factor profiles in a metered fed closely intermeshing counter-rotating twin screw extruder. Int Polym Process 22:198–203. https://doi.org/10.1515/ipp-2007-0011
18. Van Der Goot AJ, Poorter O, Janssen LPBM (1998) Determination of the degree of fill in a counter-rotating twin screw extruder. Polym Eng Sci 38:1193–1198. https://doi.org/10.1002/pen.10287

19. Mudalamane R, Bigio DI (2004) Experimental characterization of fill length behavior in extruders. Polym Eng Sci 44:557–563. https://doi.org/10.1002/pen.20050

20. Taki K, Sugiyama T, Ohara M et al (2019) Online monitoring of the degree of fill in a rotating full-flight screw of a corotating twin-screw extruder. AIChE J 65:326–333. https://doi.org/10.1002/aic.16382

21. Ahmed I, Chandy AJ (2019) 3D numerical investigations of the effect of fill factor on dispersive and distributive mixing of rubber under non-isothermal conditions: numerical investigations of the effect of fill factor. Polym Eng Sci 59:535–546. https://doi.org/10.1002/pen.24963

22. Zhu W, Jaluria Y (2001) Residence time and conversion in the extrusion of chemically reactive materials. Polym Eng Sci 41:1280–1291. https://doi.org/10.1002/pen.10828

23. Bi C, Jiang B (2009) Study of residence time distribution in a reciprocating single-screw pin-barrel extruder. J Mater Process Technol 209:4147–4153. https://doi.org/10.1016/j.jmatprotec.2008.10.006

24. Michelangelli OP, Gaspar-Cunha A, Covas JA (2014) The influence of pellet–barrel friction on the granular transport in a single screw extruder. Powder Technol 264:401–408. https://doi.org/10.1016/j.powtec.2014.05.066

25. Mateo-Ortiz D, Villanueva-Lopez V, Muddu SV et al (2021) Dry powder mixing is feasible in continuous twin screw extruder: towards lean extrusion process for oral solid dosage manufacturing. AAPS PharmSciTech 22:249. https://doi.org/10.1208/s12249-021-02148-x

26. Bauer H, Matić J, Evans RC et al (2022) Determining local residence time distributions in twin-screw extruder elements via smoothed particle hydrodynamics. Chem Eng Sci 247:117029. https://doi.org/10.1016/j.ces.2021.117029

27. Mehranpour M, Nazokdast H, Dabir B (2004) Prediction of residence time distribution for different screw configurations of a Ko-kneader by using a cluster model. Int Polym Process 19:13–15. https://doi.org/10.3139/217.1758

28. Sun D, Zhou C, Yu H et al (2022) Integrated numerical simulation and quality attributes of soybean protein isolate extrusion under different screw speeds and combinations. Innov Food Sci Emerg Technol 79:103053. https://doi.org/10.1016/j.ifset.2022.103053

29. Gao J, Walsh GC, Bigio D et al (1999) Residence-time distribution model for twin-screw extruders. AIChE J 45:2541–2549. https://doi.org/10.1002/aic.690451210

30. (2020) Hydroxypropyl methylcellulose: overview and applications. https://www.celotech.com/about-celotech/hydroxypropyl-methylcellulose-overview-and-applications.html. Accessed 22 Feb 2023

31. Richards G (1991) Aluminum oxide ceramics. In: Concise Encyclopedia of Advanced Ceramic Materials. Elsevier, pp 16–20

32. Morrison FA (2001) Understanding rheology. Oxford University Press, New York

33. stablemicrosystems.com. In: TA. HDplusC Texture Analyser. https://www.stablemicrosystems.com/TAHDplus.html

34. Corrections of Capillary Rheometer Experiments. In: https://www.goettfert.com/. https://www.goettfert.com/application-knowledge/rheo-info/for-capillary-rheometer/corrections-of-capillary-rheometer-experiments

35. Laenger K-F, Laenger F, Geiger K (2016) Wall slip of ceramic extrusion bodies, Part 2*. Process Eng 93(4–5):1–6

36. Khan AU, Briscoe BJ, Luckham PF (2001) Evaluation of slip in capillary extrusion of ceramic pastes. J Eur Ceram Soc 21:483–491. https://doi.org/10.1016/S0955-2219(00)00213-2

37. Herschel WH, Bulkley R (1926) Konsistenzmessungen von Gummi-Benzollösungen. Kolloid-Zeitschrift 39:291–300. https://doi.org/10.1007/BF01432034

38. Bingham EC (1916) An investigation of the laws of plastic flow. Bull Natl Bur Stand 13:309. https://doi.org/10.6028/bulletin.304

39. Whyman S, Arif KM, Potgieter J (2018) Design and development of an extrusion system for 3D printing biopolymer pellets. Int J Adv Manuf Technol 96:3417–3428. https://doi.org/10.1007/s00170-018-1843-y

40. Fogler HS Distributions of residence times for chemical reactors, 4th edn. Prentice Hall India Learning Private Limited, pp 868–944

41. Kumar A, Ganjyal GM, Jones DD, Hanna MA (2008) Modeling residence time distribution in a twin-screw extruder as a series of ideal steady-state flow reactors. J Food Eng 84:441–448. https://doi.org/10.1016/j.jfoodeng.2007.06.017

42. Jager T, Santbulte P, van Zuilichem DJ (1995) Residence time distribution in kneading extruders. J Food Eng 24:285–294. https://doi.org/10.1016/0260-8774(95)90047-F

43. Vergnes B (2011) Calculation of average residence time in a Ko-kneader. Int Polym Process 26:587–589. https://doi.org/10.3139/217.2528

44. FLOW-3D ((n.d.)).) Solving the world's toughest CFD problems. (FLOW Sci

45. Hirt CW, Nichols BD (1981) Volume of fluid (VOF) method for the dynamics of free boundaries. J Comput Phys 39:201–225. https://doi.org/10.1016/0021-9991(81)90145-5

46. do Amaral JV, de Carvalho Miranda R, Montevechi JA, dos Santos CH, Gabriel GT (2022) Metamodeling-based simulation optimization in manufacturing problems: a comparative study. Int J Adv Manuf Technol 120:5205–5224. https://doi.org/10.1007/s00170-022-09072-9

47. do Amaral JV, Montevechi JA, de Carvalho Miranda R, de Sousa Junior WT (2022) Metamodel-based simulation optimization: a systematic literature review. Simul Model Pract Theory 114:102403. https://doi.org/10.1016/j.simpat.2021.102403

48. Barbara R, Lorenzo D, Luca T (2017) Multi-goal optimization of industrial extrusion dies by means of meta-models. Int J Adv Manuf Technol 88:3281–3293. https://doi.org/10.1007/s00170-016-9009-2